# Locating and characterizing a crack in concrete with diffuse ultrasound: A four-point bending test

Éric Larose, Anne Obermann, Angela Digulescu, Thomas Planès, Jean François Chaix, Frédéric Mazerolle, Gautier Moreau

# Locating and characterizing a crack in concrete with diffuse ultrasound: A four-point bending test

Eric Larose[a)]
*ISTerre, CNRS, BP 53, 38041 Grenoble cedex 9, France*

Anne Obermann
*Swiss Seismological Service, ETH Zurich, Switzerland*

Angela Digulescu
*Grenoble Institute of Technology, GIPSA-lab, Saint Martin DHeres, France*

Thomas Planès
*Department of Civil and Environmental Engineering, Colorado School of Mines, Golden, Colorado 80401, USA*

Jean-Francois Chaix and Frédéric Mazerolle
*LMA, UPR CNRS 7051, Univ. Aix-Marseille, Marseille, France*

Gautier Moreau
*EDF R&D, EDF Lab., Chatou, France*

This paper describes an original imaging technique, named Locadiff, that benefits from the diffuse effect of ultrasound waves in concrete to detect and locate mechanical changes associated with the opening of pre-existing cracks, and/or to the development of diffuse damage at the tip of the crack. After giving a brief overview of the theoretical model to describe the decorrelation of diffuse wave-forms induced by a local change, the article introduces the inversion procedure that produces the three dimensional maps of density of changes. These maps are interpreted in terms of mechanical changes, fracture opening, and damage development. In addition, each fracture is characterized by its effective scattering cross section.

## I. INTRODUCTION

Mechanical waves, including ultrasound, are natural candidates for probing the mechanical properties of a material under test. Applications based on elastic or acoustic waves recorded in reflection or transmission configurations are widespread in every-day life: medical imaging, non-destructive testing, seismic imaging, etc. Concrete structures, which are widely used, constitute a large and significant application area for non-destructive evaluation and imaging techniques (Bungey *et al.*, 2006; Popovics and Rose, 1994). In some materials like multi-composite ones, including concrete (McCann and Forde, 2001), ultrasonic techniques have strong limitations when the frequency is increased. Limitations are due to two different physical phenomena: (1) absorption due to viscous-like effects is known to be very high in media containing fluids, at least partially (porous material for instance); (2) attenuation due to multiple scattering. The latter phenomenon does not kill the ultrasound waves, but transforms them into long-lasting waveforms arriving later in the record, forming the so-called ultrasonic *coda* (Derode *et al.*, 1995; Page *et al.*, 1999). The term *coda* comes from the seismology community (Aki, 1969), where it initially denoted wave trains arriving after the ballistic waves. In the mesoscopic frequency regime, where the wavelength is shorter than the size of the heterogeneities, multiple scattering has been reported (Anugonda *et al.*, 2001). In practice, this regime develops at frequencies higher than 100–150 kHz for concrete formulations that include centimetric gravel. For more details on the limitation of existing techniques in the mesoscopic regime, we refer the reader to Planes and Larose (2013). Turning these random-like long-lasting waveforms into relevant information on the nature of the material and its time-dependent change is a real challenge!

This paper describes an original imaging technique that benefits from ultrasound waves that have undergone multiple scattering in concrete to detect and locate mechanical changes. These changes are associated with the re-opening of pre-existing cracks, and/or to the development of diffuse damage at the tip of the crack. Section II describes the preparation of the four test samples and the mechanical experiment. Details are then given of the ultrasonic data acquisition procedure. Section III gives an explanation of how to measure the quantities that are relevant to structural changes in the material, i.e., the decorrelation of diffuse ultrasonic waveforms. Section IV gives a brief overview of the theoretical model for predicting the decorrelation induced by a local change. Section V gives details of the inversion

[a)]Also at: ISTerre, Univ. de Grenoble Alpes, BP 53, 38041 Grenoble cedex 9, France. Electronic mail: eric.larose@ujf-grenoble.fr

TABLE I. Concrete composition.

| Component | Mass (kg/m$^3$) |
|---|---|
| Cement CEM I 52.5 N | 370 |
| Sand 0/4 mm | 774 |
| Aggregate SR 4/14 mm | 1069 |
| Water (w/c = 0.57) | 212 |

TABLE II. Measured crack depth (surface microscope).

| Sample No. | Crack depth before | Crack depth after |
|---|---|---|
| 1 | notch only | notch only |
| 2 | 23 mm | 25 mm |
| 3 | 30 mm | 37 mm |
| 4 | 50 mm | 60 mm |

procedure that produces the three dimensional (3D) maps of density of changes, and the associated resolution. Section VI proposes a possible interpretation of these maps in terms of mechanical changes, fracture opening, and damage development. The characteristics of each fracture are also determined. The concluding section summarizes the main findings of the paper and suggests future ideas for further development of the Locadiff imaging procedure.

## II. EXPERIMENTAL SETUP

### A. Sample preparation

Four concrete samples of size 150 mm × 120 mm × 600 mm were prepared several weeks before the test. The concrete formulation is given in Table I and is a typical formulation used in civil engineering.

A 1 cm deep notch was created in the middle of each sample (see Fig. 1) to initiate the future crack. The samples then underwent a first fracturing process. This process used a three-point bending system with mechanical loading controlled by the opening of the crack. Each test was stopped for different crack depths. The crack depths were measured by optical observations with a microscope (of magnification 60×) and a simple ruler. Cracks of various depths were obtained, ranging from 0 mm (intact) to 23, 30, and 50 mm.

### B. The four-point bending test

A four-point bending test was performed on each sample, one after the other. Each sample was placed in the same apparatus (see Fig. 1). The two lower bearing points were fixed on the table and the two upper bearing points moved in the vertical direction. Each bearing point was cylindrical and adapts to the specimen by small rotational movements according to the European standard for the test (NF EN 12390-5). Mechanical loading was performed by step-by-step control of the vertical displacement of the two upper fulcrums. The samples were equipped with a displacement sensor to monitor the opening of the crack. They were also equipped with a set of ultrasonic sources and receivers, distributed on one side only, around the central part of the specimen where the crack was expected to be re-opened (see Fig. 1).

The load was increased from 0 to about 10 kN by increments of about 1 kN, and then released. After each test, new optical observations were taken to evaluate the slight increase in crack depth (see Table II).

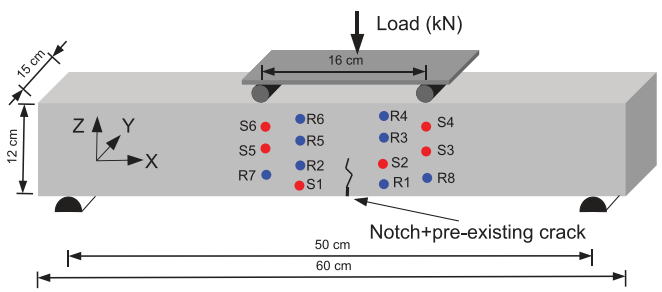


FIG. 1. Experimental apparatus. R1-8 label the position of the height ultrasonic receivers, and S1–S8 label the position of the sources. Sources and receivers are operated in the 500–900 kHz frequency range. Transducers are placed sparsely to cover the surface to image, with no additional position requirements.

### C. Ultrasonic data acquisition

At each load step $k$, all the ultrasound impulse responses $h_{ij}(t)$ were acquired. The sources $S_i$ were excited one at a time with a chirp $s(t)$ of frequencies ranging linearly from 500 to 900 kHz. The chirp amplitude was +/−2 V, and the duration was 5 ms. The waveforms recorded at the receivers $Rj$ are noted $r_{ij}(t)$. The excitation was reproduced 200 times and records were stacked accordingly. The waveforms were simultaneously recorded on all the available eight receivers $j$: $r_{ij}(t) = h_{ij}(t) \otimes s(t)$, where $\otimes$ stands for convolution. Assuming that the source spectrum is broad enough such that $s(t) \times s(s) \approx \delta(t)$, where $\times$ stands for correlation, we further correlated the records with the source function to evaluate the impulse response in the working frequency band:

$$h_{ij}(t) \approx r_{ij}(t) \times s(t). \quad (1)$$

In Fig. 2(a) an example of impulse response is illustrated, showing the main characteristics of multiple-scattered waves: the direct wave is strongly attenuated, and is followed by a long-lasting coda with an average amplitude (the envelope) that is well described by the solution of the diffusion equation. In an infinite medium, the equation of the intensity [noted $I_\infty(r, t)$] takes the well-known form of

$$\partial_t I_\infty(r,t) - D\Delta I_\infty(r,t) - 1/\tau_{abs} I_\infty(r,t) = s^2(r,t), \quad (2)$$

where $s^2(r, t)$ is the source intensity at time $t$ and position $r$. In our finite sample, assuming perfectly reflecting boundaries, the diffusion solution is evaluated as the sum of several infinite medium solutions corresponding to different mirror images of the source. Each of these mirror-imaged sources accounts for a specific number of reflections on the sample boundaries. The fit parameters obtained on the envelope using perfect reflections at the sides are the diffusivity $D = 12\,\mathrm{mm}^2/\mu\mathrm{s}$, and the absorption time $\tau_{\mathrm{abs}}$ of 25 $\mu$s. Note

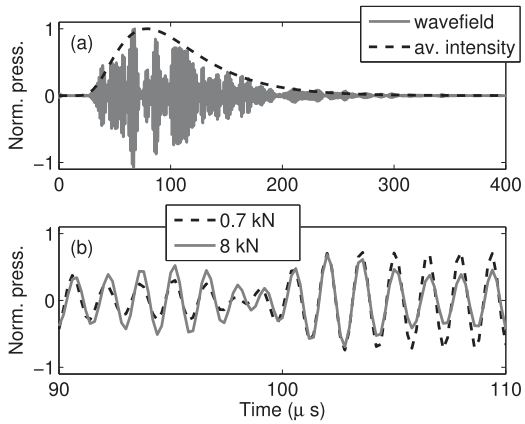


FIG. 2. Example of ultrasonic impulse responses acquired in the concrete sample in the 500–900 kHz frequency range between source 6 and receiver 8 with the 23 mm pre-cracked sample. (a) Full wave field (solid line) and average intensity (broken line). The diffuse regime is characterized by the attenuation of the direct wave, and by the onset of the late and long-lasting ultrasonic coda. (b) Zoom on the coda. The two waveforms are acquired with a fixed source and receiver but at different mechanical load. The decorrelation is mainly due to the opening of the crack as a result of the four points bending loading.

that the following imaging procedure does not need an estimate of the absorption time, and requires only a rough estimate of the diffusion constant. Consequently, there is no point in making a precise evaluation of these quantities (Rossetto *et al*., 2011).

The ultrasonic impulse response $h_{ij}$ represents the ultrasonic fingerprint of the medium. If the material should change in any way, even far away from the source–receiver segment, the ultrasonic fingerprint potentially changes accordingly, as illustrated in Fig. 2(b).

## III. DATA PROCESSING

The initial level of applied force is considered to be the reference level. During the experiment, two physical phenomena may lead to a slight increase in ultrasonic velocities: the change in temperature (Larose *et al*., 2006) and the change in stress (acousto-elasticity, Larose and Hall, 2009). In an attempt to correct the waveforms with regard to these effects, the waveforms were interpolated with various stretching factors $\varepsilon$: $h_{i,j}(t) \rightarrow h_{i,j}[t(1+\varepsilon)]$, in order to find the stretching factor that makes the current impulse response ($h^k$) best resemble the reference impulse response ($h^{\mathrm{ref}}$) (Lobkis and Weaver, 2003; Sens-Schönfelder and Wegler, 2006; Sens-Schönfelder and Larose, 2008). In practice, the actual relative velocity change $\varepsilon = dV/V$ is the stretching factor that maximizes the following cross-correlation coefficient:

$$CC_{i,j}(\varepsilon,k,t)=\frac{\int_{t-(T/2)}^{t+(T/2)} h_{i,j}^{\mathrm{ref}}(\tau)h_{i,j}^{k}[\tau(1+\varepsilon)]d\tau}{\sqrt{\int_{t-(T/2)}^{t+(T/2)} h_{i,j}^{\mathrm{ref}}(\tau)^2 d\tau \int_{t-(T/2)}^{t+(T/2)} h_{i,j}^{k}[\tau(1+\varepsilon)]^2 d\tau}}, \quad (3)$$

where $T$ is the time window centered on time $t$ in the coda. In practice, a time-window of duration $T = 50\,\mu$s is chosen, centered at different times $t = 50$, 100, 150, and 200 $\mu$s. The choice of $T$ is a trend between time averaging to stabilize the measure of the correlation coefficient (thus $T$ should be much larger than the central period), and time resolution in the coda ($T$ should be small compared to the total duration of the record). The global $dV/V$ obtained in the sample corresponds to a very limited temperature change (much smaller than 1 °C over the experiment), which is consistent with the limited thermal variations observed in the room during the experiment and the thermal diffusivity in the concrete sample. Note that, to perform a perfect correction of temperature effect (thermal bias control), it would also be possible to use an additional concrete sample free of mechanical solicitation, following Zhang *et al*. (2012).

For each load step $k$ the experimental decorrelation between the reference impulse response $h_{i,j}^{\mathrm{ref}}(t)$ and the corrected current impulse response $h_{i,j}^{k}[t(1+\varepsilon_{\max})]$ is calculated

$$DC_{i,j}(k,t) = 1 - CC(\varepsilon_{\max},k,t). \quad (4)$$

A decorrelation of 0 means that waveforms are perfectly similar. A value of unity is obtained for perfectly uncorrelated (dissimilar) waveforms. This experimental decorrelation is plotted on Fig. 3 for each load step $k$ and for the four specimens, after averaging on all source–receiver pairs at time $t = 150\,\mu$s in the coda. Note that, in general, decorrelation values vary with the position of the sensors ($i$, $j$), the time in the coda $t$, and the crack opening (or level of damage).

## IV. THEORETICAL PREDICTION FOR THE DECORRELATION

Following previous theoretical and numerical studies (Planès, 2013; Planès *et al*., 2014; Rossetto *et al*., 2011), we can estimate a theoretical value of the decorrelation assuming a punctual defect of scattering cross-section $\sigma$ appearing at position x:

$$DC_{i,j}^{Th}(\mathrm{x},t) = \frac{c\sigma}{2} K_{i,j}(\mathrm{x},\mathrm{t}), \quad (5)$$

where $c$ is the transport velocity of the ultrasonic intensity (the shear wave speed as a first approximation), and $K_{ij}$(x, t) the sensitivity kernel. This sensitivity kernel represents the

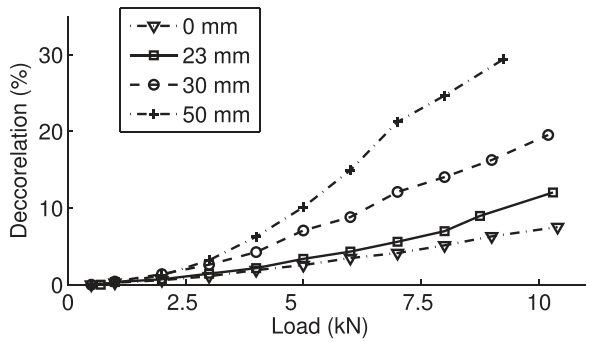


FIG. 3. Decorrelation of ultrasonic coda waves obtained for various initial crack sizes, and for various loads. The larger the pre-existing crack, the greater the decorrelation. Decorrelations are obtained at $t = 150\,\mu$s in the coda, average in a 50 $\mu$s-long time window, and then averaged over all available source receiver positions.

probability of a wave packet launched at the source $i$ at time 0 and received at time $t$ at receiver $j$ passing by the location x and interacting with the defect. It is defined as

$$K_{i,j}(\mathrm{x},t)=\frac{\int_o^t I(i,\mathrm{x},u)I(\mathrm{x},j,t-u)du}{I(i,j,t)}, \tag{6}$$

where $I(i, j, t)$ is the probability of transport from $i$ to $j$ after a time $t$, which simply connects to the average intensity recorded in $j$ after a source in $i$ and after a propagation time $t$. In the present work, the intensity is approximated by the solution of the diffusion equation [see Eq. (2)] including perfect reflections at the sides. This solution is known to be valid if the source, receiver, and defect are far away from each other (more than one scattering mean free path in practice). Consequently, the possibility of an error must be acknowledged if the source/receiver/defect are closer than the mean free path, but in practice the sources and receivers are placed further from each other, and also further from the pre-existing crack. Note that when the position of the defect is absolutely unknown, the solution of the radiative transfer equation should alternatively be employed (Planès *et al.*, 2014).

In the present paper, the numerical estimation of the solution of the diffusion equation takes into account the multiple reflections on the sides of the sample, assuming a perfect reflection condition. Note that the perfect reflection condition and the estimation of the diffusivity (or scattering mean free path) are rather approximate, but results presented in the following of the paper (crack location and estimated crack size) are found to be only slightly dependent on these parameters (Rossetto *et al.*, 2011).

## V. INVERSION PROCEDURE AND EXPERIMENTAL RESULTS

### A. Inversion procedure

To estimate the volumetric distribution of the changes [density map $\sigma(\mathrm{x})$ of the scattering cross-section of the change], we assume that the total decorrelation probed by the sensors is a linear function of the decorrelation induced by each individual change $\sigma(\mathrm{x})$ in the elementary volume $\delta V$ (x):

$$DC_{ij}(t)=\frac{c}{2}\oint\sigma(\mathrm{x})K_{ij}(\mathrm{x},t)\delta V(\mathrm{x}), \tag{7}$$

where the integral is performed over the whole volume of the sample. Note that this formulation does not include multiple reflections of ultrasound waves between different parts of the crack, such that this formulation is only a first order approximation. This formulation is thus not suitable for changes much larger than the wavelength or collections of close changes, but has the major advantage of being easy to implement numerically.

The sample was split into elementary cells (voxel) of size $\delta V = 1\,\mathrm{cm}\times 1\,\mathrm{cm}\times 1\,\mathrm{cm}$. In matrix form, the direct problem can now be written as (Obermann *et al.*, 2013; Planès, 2013; Planès *et al.*, 2014)

$$\boldsymbol{DC}=\frac{c\delta V}{2}\mathbf{K}\boldsymbol{\sigma}, \tag{8}$$

where $\boldsymbol{DC}$ is the vector whose component $DC_p$ corresponds to the decorrelation measurements $p$ for a given pair at a given time $t$, $\boldsymbol{K}$ is the matrix of the sensitivity kernels whose elements $K_{pq}$, for a given source–receiver pair and time $p$ at each voxel $q$, are evaluated following Eq. (6), and $\sigma$ is the vector whose elements $\sigma_q$ are the scattering cross-sections of the model for each voxel $q$. Note that the decorrelation vector $\boldsymbol{DC}$ can include data obtained at different times $t$ in the coda.

To solve the inverse problem for $\boldsymbol{\sigma}$, we use a formulation of the least-squares method for linear problems proposed by Tarantola and Valette (1982):

$$\boldsymbol{\sigma}=\boldsymbol{\sigma^0}+\boldsymbol{C}^m\boldsymbol{K}^+(\boldsymbol{G}\boldsymbol{C}^m\boldsymbol{K}^++\boldsymbol{C}^d)^{-1}(\boldsymbol{DC}-\boldsymbol{K}\boldsymbol{\sigma^0}), \tag{9}$$

where $\boldsymbol{\sigma^0}$ is the initial model: a zero vector in this case since there is no *a priori* information about the position, size and number of cracks. In addition, $\boldsymbol{G}=(c\delta V/2)\boldsymbol{K}$. $\boldsymbol{C}^d$ is noted as the covariance matrix for the data, which represents uncertainties and correlations of the decorrelation measurements $\boldsymbol{DC}$. The exponent $^+$ holds for matrix transposition. $\boldsymbol{C}^m$ is the covariance matrix for the model, i.e., the spatial fluctuations of the expected $\boldsymbol{\sigma}$ values. To limit the number of independent parameters, a spatial smoothing procedure is performed on the model, obtained from correlations of neighboring cells.

As the scattering cross-section is necessarily positive, an iterative procedure is introduced that imposes a positivity constraint. Therefore, at each iteration step, only positive values are kept and used as new input data for the model. In this study, height iteration steps are used. The requested calculation time was $48\times 8$ min for the sensitivity kernels, and 1 min for an inversion with eight iterations, using a single core standard desktop computer.

### B. Inversion parameter and resolution map inversion parameter

Further details of the procedure used to define the matrix $\boldsymbol{C}^m$ are given below. Each element $ij$ of this matrix is defined as

$$C^m(i,j)=\left(std^m\frac{L_0}{L}\right)^2 e^{-r/L}, \tag{10}$$

where $L_0$ is the size of the elementary cell and $L$ the length of spatial smoothing, and $std^m$ is the allowed fluctuation of the model. $L$ and $std^m$ are tunable parameters of the inversion. Also, $r$ is the distance between cells $i$ and $j$. The longer $L$, the greater the smoothing (spatial averaging). Smoothing is necessary as, in most cases, the inverse problem is underdetermined. An optimum trade-off therefore needs to be determined between spatial smoothing ($L$) and expected fluctuations ($std^m$), following the work of Hansen (1992). The best (or most significant) couple of parameters is found by

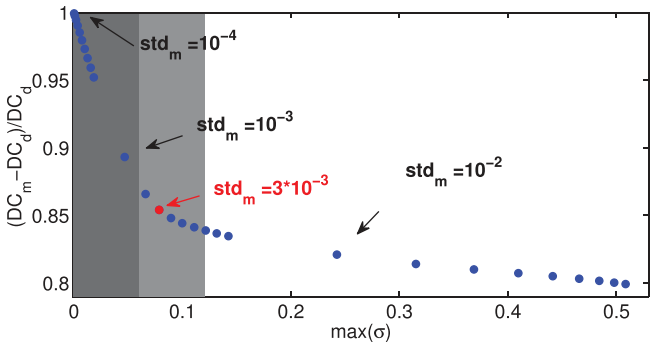


FIG. 4. Search of optimal inversion parameter $std_m$ ($L$-curve test) for a given value of spatial smoothing of $L = 30$ mm. The dark part corresponds to low fluctuations allowed in the model, yielding to a high misfit between experimental data and the model. On the opposite, the white part corresponds to very high allowed fluctuations, which allow us to reduce the misfit without better significance. The best compromise is obtained at the corner of the slop, at the red point for $std^m = 3 \times 10^{-3}$.

performing an *L-curve* test, displayed in Fig. 4. In this figure, the normalized misfit between the data $\boldsymbol{DC}^{\boldsymbol{d}}$ and the decorrelation predicted by the model $\boldsymbol{DC}^{\boldsymbol{m}} = (c\delta V/2)\boldsymbol{K\sigma}$ is plotted versus the maximum fluctuation of the model $\sigma$ for different values of $std^m$, and for $L = 30$ mm (other values for $L$ were also tested). The dark part corresponds to a strong smoothing where the misfit is high and the allowed fluctuations too limited. The white part corresponds to a very limited misfit but fluctuations of the model are very large. In both cases results of the inversion are less probable. The most significant inversion parameters are found at the corner of the slope (in red) for an *a priori* variance of the model of $std^m = 3 \times 10^{-3}$.

### 1. Resolution map

The inversion is performed on an area centered around the crack, including the whole sample along the $Y$ and $Z$ axes. For computational reasons, the inversion is limited along the $X$ axis to $X = +20$ cm to $X = +40$ cm. To confirm the efficiency of the inversion result in such a volume, the model resolution is considered. The resolution operator is defined as

$$\boldsymbol{R} = \boldsymbol{I} - \{(C^m)^{-1} + [\boldsymbol{G}^{+}(C^d)]^{-1}\boldsymbol{G}\}^{-1}(C^m)^{-1}, \qquad (11)$$

where $\boldsymbol{I}$ is the identity in the model space. $\boldsymbol{R}$ relates the resulting model correction $\boldsymbol{\sigma}^m$ to the true model correction $\boldsymbol{\sigma}$ according to Tarantola and Valette (1982): $\boldsymbol{\sigma}^m = \boldsymbol{R}(\boldsymbol{\sigma}) + noise$, where the *noise* term comes from the discrepancy between true and observed data.

Of particular interest is the averaging index (Vergely *et al.*, 2010) which, given a cell $i$, is defined as the sum of the coefficients $R_{ij}$ of the line $j$ in the resolution matrix. When the averaging index is close to 1 (or in practice greater than 0.7), the resulting value of the model approximately corresponds to a spatial average of the true model. More details can be found by consulting additional references (Obermann *et al.*, 2014). Figure 5 displays the averaging index $R$, indicating that the resolution is good in the $X$-$Z$ plane (perpendicular to the crack) but with a satisfactory resolution along the $Y$-axis for $Y = 0$ cm to 6 cm only. The lack of resolution for $Y > 6$ cm results from the limited penetration of diffuse ultrasound at the working frequencies. In the following, only the density maps $\sigma$ where $R > 0.5$, are displayed and interpreted and the other regions are masked.

### C. Experimental results

The mechanical behavior of the samples is as follows. Two vertical forces are applied in the $Z$ direction along two lines ($Y$ direction) around the middle of the top surface of the samples (above the notches, see Fig. 1). The notches were performed in the middle of the bottom face, in the $Y$ direction. The cracks were performed before the current experiment and developed from the notch in the $Z$ direction, approximately along the $Y$-$Z$ plane. The depth of the cracks was evaluated from visual inspection on each lateral $X$-$Z$ faces before, and after the current experiment, and are reported in Table II. During the loads, cracks re-open in the $X$ direction, starting from the bottom face. Thus they re-open more on the bottom surface than in the core. We follow the opening of the cracks by measuring the horizontal elongation (along the $X$ direction) between each rim of the notches at the bottom face, and report the results in Fig. 6.

Also, the crack depths after the experiment were found slightly larger than before, which demonstrates that incremental cracking occurred at the tip of the pre-existing fractures during the load. As Locadiff is sensitive to mechanical changes in the material, we hope to be able to visualize pre-existing cracks as they re-open, and possibly additional cracking. This visualization is performed in the bulk of the samples. The purpose of the present paper is to evaluate if we locate properly the pre-existing cracks, and if we can characterize them.

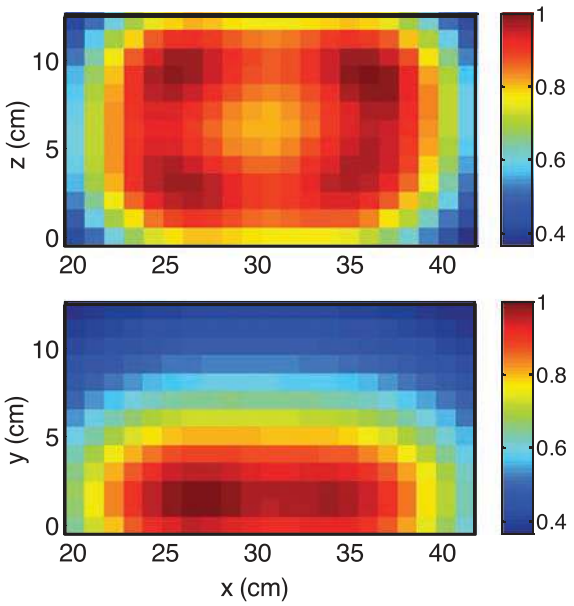


FIG. 5. Resolution map. Top: in the $X$-$Z$ plane, resolution evaluated at the surface of the sample (on transducer side). The resolution is relatively homogeneous in this plane, with values greater than 0.7. Bottom: horizontal cut ($X$-$Y$ plane) in the middle of the sample. The resolution is satisfactory for $Y < 6$ cm.

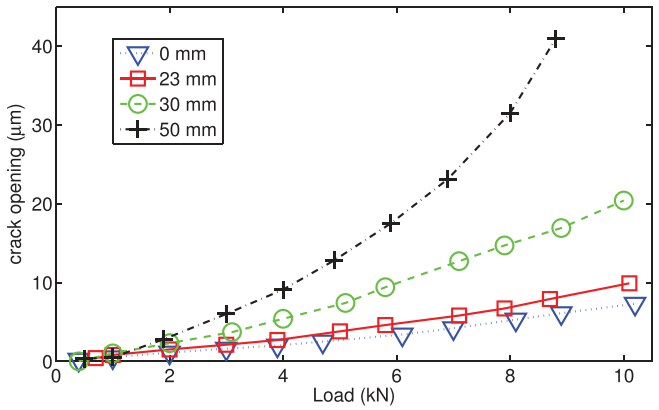


FIG. 6. Horizontal ($X$ axis) elongation at the rims of the notches during the loads of the four samples. The depth of the pre-existing crack is reported in the top left panel. The deeper the pre-existing crack, the larger the opening at the bottom face. The elongation includes the elastic response of the sample during bending, and (mostly) the crack opening at the bottom surface.

The results of the inversion are given hereafter: maps are produced showing the density of scattering cross-section of the changes, performed at various loads and on the four specimens, following Eq. (9). In Fig. 7, maps of the changes are plotted for the sample with a 23 mm pre-existing crack, at various loads. The maps are vertical slices ($X$-$Z$ plane, see Fig. 1) performed $Y = 1$ cm beneath the surface. Similar maps are obtained at other depths ($Y = 2$ cm to $Y = 6$ cm). The grey scale represents the scattering cross-section of the changes in each pixel, in mm$^2$/mm$^3$. The changes are located properly around the pre-existing crack, and the intensity of the change increases with load, and thus fracture opening and possibly damage at the tip of the crack. Qualitatively, the change is thus properly located by the technique, and the general trend (increase of change intensity with crack opening) is recovered. The extension of the spot in the images is nevertheless large compared to the real opening length of the crack, the resolution is indeed limited by the diffusion process in the material. In other words, the spatial resolution is on the order of the scattering mean free path, corresponding to a few centimeters (much larger than the few tens of micrometers of crack opening).

Figure 8 represents a horizontal cut of the same maps chosen at $Z = 2$ cm immediately above the notch at the elevation of the fracture. The areas with insignificant resolution are shown in yellow. The changes are approximately located around the real crack, with a horizontal spread of a few centimeters due to the spreading of the sensitivity kernels and to the spatial smoothing of the inversion process (3 cm). Again, the position of the changes corresponds to the position of the crack, and the absolute intensity increases with load. The asymmetry along the $Y$-axis is only due to depth penetration issues (to be discussed in the conclusion section).

Figures 9 and 10 show plots of similar maps ($X$-$Z$ and $X$-$Y$ cuts) obtained for the four samples with increasing pre-existing crack depth, at the same load level (7 kN). The changes are found to correspond well to the actual position of the crack, with a resolution of about 3–5 cm in each direction. The absolute intensity of the change increases with increasing crack size. The slight asymmetry comes from the random position of the sensors and the slight experimental error in the estimation of the decorrelation. Note that the absence of any signal for the sample without an initial crack is only due to the normalization of the color scale. When zooming into lower levels of scattering cross-sections, changes at the position of the notch can be clearly located. With this sample, it may appear confusing that changes are observed without any macroscopic crack; comments on this observation will be given in Secs. V D and VI.

To conclude on these first experimental results, Figs. 7–10 demonstrate that the Locadiff technique can properly recover the position of pre-existing cracks in the bulk of the samples under loading test, with a precision of a few centimeters. It has also been demonstrated that the observed intensity of the change, measured in terms of scattering cross-section (units in mm$^2$/mm$^3$), qualitatively relates to the crack size, and also to the load. In the final section, the quantitative relationship between the cross-section of the change and the actual size of the crack is discussed.

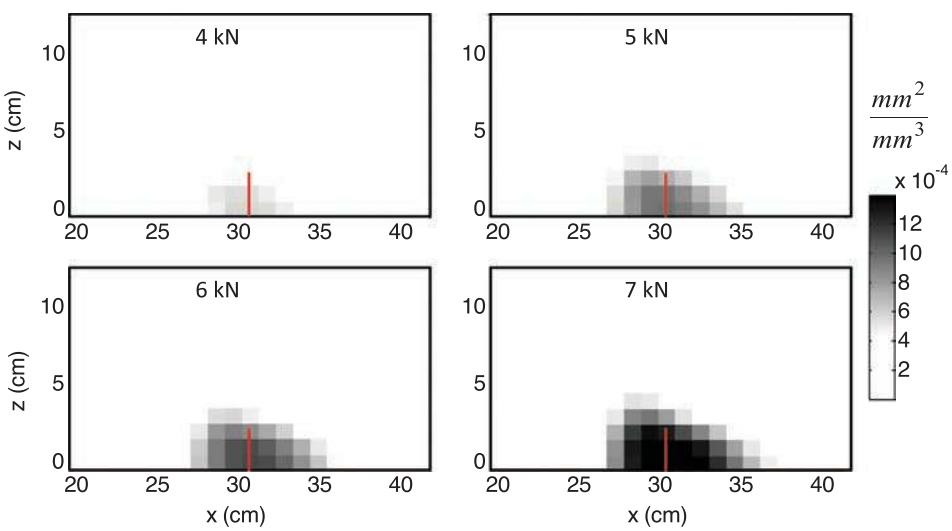


FIG. 7. Map of scattering cross-section density $\sigma$ in the $X$-$Z$ plane, obtained at different loads ranging from 4 to 7 kN at $Y = 1$ cm. The height of the pre-existing crack (23 mm) is inserted in each plot with a red line.

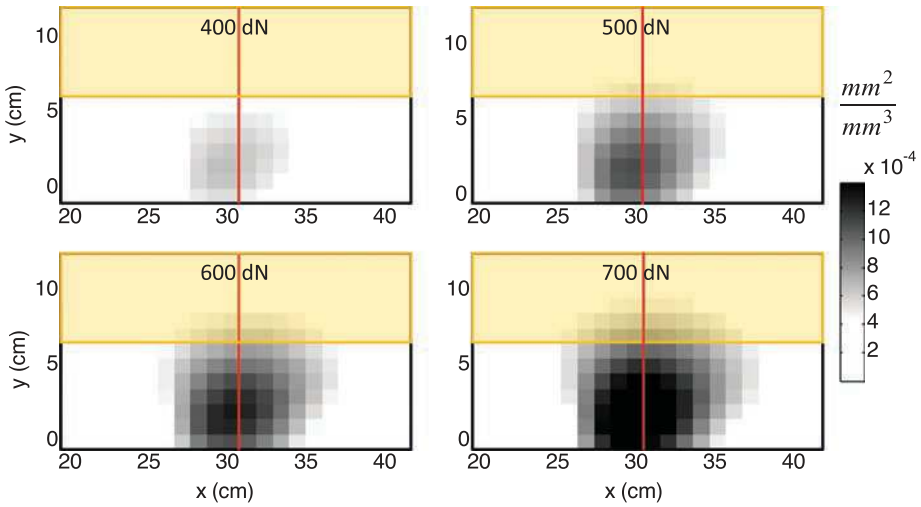


FIG. 8. Map of scattering cross-section density $\sigma$ in the $X$-$Y$ plane, obtained at different loads ranging from 4 to 7 kN ($Z = 2$ cm). The position of the pre-existing crack is inserted in each plot with a red line. Areas of insignificant resolution are shown in yellow.

### D. Total scattering cross-section of the change, and estimation of crack size

For practical applications, it is not only the position of the crack that needs to be imaged, but also the crack depth, or in other words, the size of the crack in the material, along with local damage around or before the crack. To see how the scattering cross-section might relate to the actual size of the crack, the scattering cross-section density is integrated over the volume that is correctly resolved (see Secs. IV and V B 1):

$$\sigma_{\text{tot}} = \iiint \sigma(x) d^3x. \tag{12}$$

Successive values of $\sigma_{\text{tot}}$ versus load for the four samples are illustrated in Fig. 11, where it can be seen that (1) $\sigma_{\text{tot}}$ increases with load; (2) $\sigma_{\text{tot}}$ increases with crack size, and (3) the absolute value of $\sigma_{\text{tot}}$ is on the order of the actual size of the crack. This figure raises at least two questions. First: does the total scattering cross-section of the change relate precisely to crack depth? Second: why is the total scattering cross-section of the non-cracked sample significantly larger than zero? These issues are addressed in the following section.

## VI. DISCUSSION AND CONCLUSION

To answer the first question raised, consider the simple case of a penny-shaped crack of limited extension. For a penny-shaped crack of diameter $L$ greater than the wavelength, the total scattering cross-section in 3D, averaged over all incoming and outgoing angles, is on the order of $\pi L^2$. In recent theoretical and numerical studies (Planès *et al.*, 2014), it has been demonstrated that the Locadiff technique can correctly quantify the cross-section of a change. For symmetry reasons, in the present experiment, the crack is expected to be continuous along the $Y$-axis (which was visually checked after the experiment). Thus, a very rough estimation of crack depth can be derived by dividing $\sigma_{\text{tot}}$ by the length along the $Y$-axis (within the resolved volume): 6 cm. Values of a few centimetres are obtained, which is the

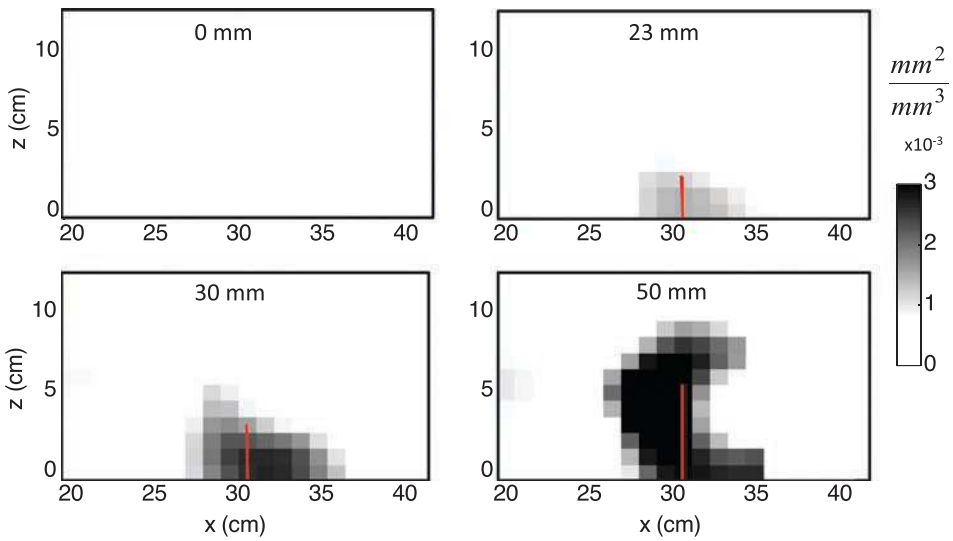


FIG. 9. Maps of scattering cross-section density $\sigma$ in the $X$-$Z$ plane, obtained at 7 kN (at $Y = 1$ cm). The height of the pre-existing crack is inserted in each plot (0 – 23 – 30 – 50 mm, respectively) with a red line at the crack position. The black and white color scale is fixed and normalized for all the four images. The first image is blank since the scattering cross section (mechanical change) for a non-cracked sample is very weak compared to the others.

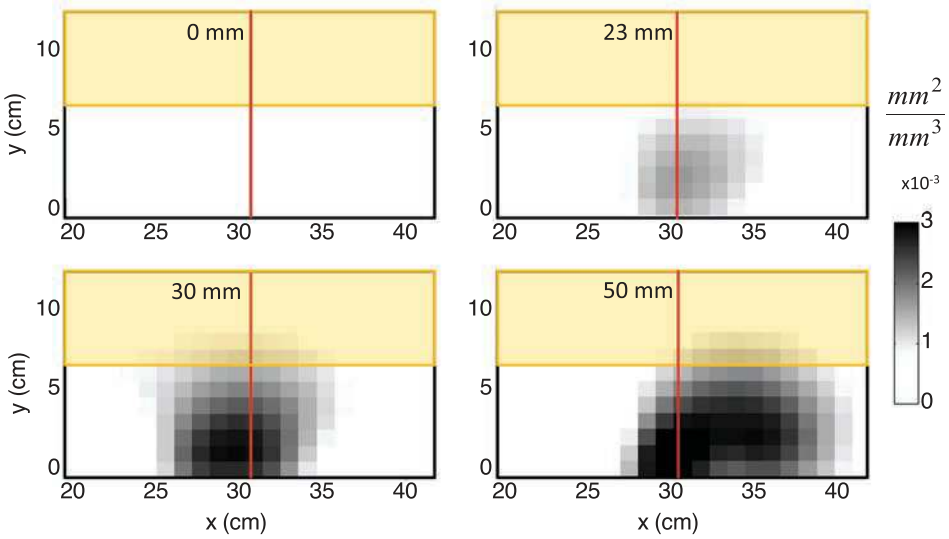


FIG. 10. Maps of scattering cross-section density $\sigma$ in the $X$-$Y$ plane, obtained at 7 kN ($Z = 2$ cm). The position of the pre-existing crack is inserted in each plot with a red line. Areas of insignificant resolution are shown in yellow. The black and white color scale is fixed and normalized for all the four images. The first image is blank since the scattering cross section (mechanical change) for a non-cracked sample is very weak compare to the others.

order of magnitude of the pre-existing crack. What remains to be explained is the precise quantitative misfit, which might relate to the limitations of the current technique, or to the physics behind. The main limitations and explanations are as follows:

- Locadiff gives the scattering cross-section of the change by comparing an original and final state. To get the total scattering cross-section of the crack, the crack has to be perfectly closed in the initial state (or non-existent), and perfectly open in the final state. The values provided by the present experiment may therefore be expected to underestimate the crack size.
- For open cracks with large extension, i.e., much larger than the scattering mean free path (in this instance on the order of 14 mm), the propagation of ultrasonic intensity is significantly modified (Payan *et al.*, 2013; Quiviger *et al.*, 2012; Ramamoorthy *et al.*, 2004). In other words, the solution of Eq. (2) should not be solved with the same boundary conditions in the initial and final state, and Eq. (6) no longer applies rigorously. This may explain why the localisation of the largest crack (50 mm) is not as good as for the others.

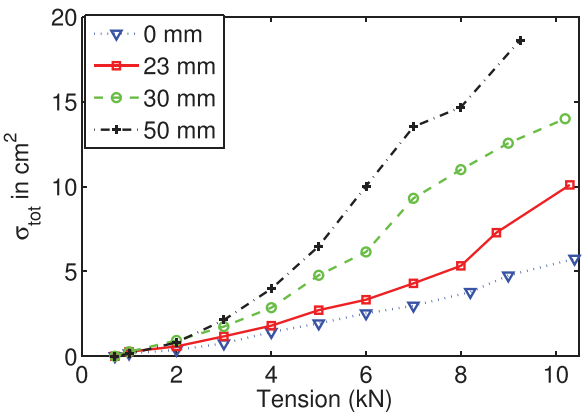


FIG. 11. Total scattering cross-section $\sigma_{tot}$ of the change integrated over 6 cm along the $Y$-axis, and over the other full axis ($X$ and $Z$).

- The observed decorrelation that fuels the Locadiff images, is simultaneously due to all the changes in the material, including the opening of macroscopic cracks, and micro-damage/micro-cracks developing at the tip of the pre-existing crack or notch. Both, micro- and macro-cracks were found to develop for the three pre-existing crack samples: see for instance the additional crack depth reported in Table II.
  Unfortunately, it is difficult to discriminate which part of $\sigma_{tot}$ is due to micro-damage at the tip, and which part of $\sigma_{tot}$ is due to the opening of the pre-existing crack. What is clear, nevertheless, is the case of the non-pre-cracked sample, where an increase in $\sigma_{tot}$ during loading can clearly be seen. In this case, as no macroscopic cracks could be seen at the end of the experiment, it may be concluded that $\sigma_{tot}$ is solely due to micro-cracking. In favor of this interpretation, it is widely observed that micro-damage is expected to concentrate at the tip of the notch.
- The total deformation of the specimen during loading slightly modifies the relative position of the heterogeneities, which leads to additional decorrelation of the waveforms. This effect would be localized mostly at the sides of the sample where the deformation is greatest, and not in the middle of the sample.

To conclude on the performance of Locadiff in these bending tests, it can be said that, at the working frequencies, Locadiff was sensitive to very small disturbances, including opening of very small cracks. It is beyond the scope of the present paper to make a quantitative comparison of Locadiff with other existing techniques, this will be the subject of additional thorough investigations. We can nevertheless draw the general following ideas concerning other techniques:

- Acoustic emission is a well established technique that allow to map appearing cracks by locating micro-cracking associated to the damage process (see, for instance, Ohtsu *et al.*, 1998 and references therein). In the present case, such a technique would have two limitations. First, in the

mesoscopic regime (high frequency ultrasound), direct waves are hardly attenuated and locating the sources would be difficult. Second, as we re-opened an existing crack, we do not expect micro-cracking (at least for first loading steps where we did not detect any additional damage).

- Ultrasonic tomography is an alternative technique (Bungey *et al*., 2006; Kepler *et al*., 2000) able to detect and locate areas of significant micro-cracking or damage. Again, attenuation of direct waves in the mesoscopic regime reduces the advantage of this technique (reduction of sensitivity to weak perturbation). Also, the spatial resolution of tomography requires having lots of sensors covering all possible paths across the volume. In comparison, Locadiff is able to locate changes in 3D with only a few sensors on one side of the sample.
- Attenuation of surface waves is another possible tool to detect and quantify cracks (see, for instance, Popovics *et al*., 2000). The depth resolution of surface waves is nevertheless limited to the wavelength. Looking at greater depth requires going at larger wavelength (lower frequency), which in general also decreases the sensitivity. As the Locadiff technique is based on 3D bulk waves, it does not suffer from the same depth sensitivity limitation.

Concerning the characterization of the cracks, or in other words the size of the open part of the crack, it was shown that a good order of magnitude could be obtained, but additional studies are required in order to determine the precise crack size and geometry, and also to discriminate between changes due to micro-damage and changes due to the opening macroscopic cracks.

For practical on-site applications, an important point to be considered is the relation between ultrasound frequency, penetration depth and size of the sample. For the relatively small sample studied here, it was decided to work at high frequency, say, between 500 and 900 kHz, with centimetric resolution but with very limited depth penetration (6 cm). Other experiments were performed at lower frequencies and indicated that the depth penetration of ultrasonic coda could be on the order of 1 m at 150 kHz (with a resolution on the order of 15 cm), which is the size range of large civil engineering structures that need to be monitored. Note that, at low frequency, the scattering mean free path is larger, and the resolution is thus greater too ($\approx$0.15 cm in the latter configuration). For Locadiff as for any other ultrasonic imaging technique, there exists a trade-off between spatial resolution and depth penetration.

In order to test the robustness of the technique, inversion procedures were also performed after removing one sensor from the dataset. The images were found to yield similar observations, though undergoing a slight reduction in spatial resolution. A major advantage of using ultrasonic coda techniques, and particularly Locadiff, is the very high sensitivity and the possibility of detecting and locating early stages of damage and micro-cracking. Another significant advantage of Locadiff, compared to many other non-destructive techniques based on superficial observations, is that it provides 3D mapping of mechanical changes in the bulk of the material.

## ACKNOWLEDGMENTS

The authors acknowledge funding from the VOR program (University J. Fourier) and from Electricite De France (EDF) Res. and Dev. The samples were provided by EDF. The experiments were performed by E.L., J.-F.C., and F.M. Ultrasonic data processing and Locadiff inversions were performed by A.O., A.D., T.P., and E.L. A.O. was funded by the European Res. Commission (ERC) Adv. Grant Whisper 227507. This work is part of the ANR-11-RSNR-0009 ENDE project, and also partially funded by the Labex OSUG@2020 (ANR10 LABX56).

Aki, K. (**1969**). "Analysis of the seismic coda of local earthquakes as scattered waves," J. Geophys. Res. **74**, 615–618, doi:10.1029/JB074i002p00615.

Anugonda, P., Wiehn, J. S., and Turner, J. A. (**2001**). "Diffusion of ultrasound in concrete," Ultrasonics **39**, 429–435.

Bungey, J. M., Millard, S. G., and Grantham, M. G. (**2006**). *Testing of Concrete in Structures*, 4th ed. (Taylor and Francis, London), pp. 1–338.

Derode, A., Roux P., and M. Fink (**1995**). "Robust acoustic time reversal with high order multiple scattering," Phys. Rev. Lett. **75**, 4206–4209.

Hansen, P. (**1992**). "Analysis of discrete ill-posed problems by means of the l-curve," SIAM Rev. **34**, 561–580.

Kepler, W. F., Bond, L. J., and Frangopol, D. M. (**2000**). "Improved assessment of mass concrete dams using acoustic travel time tomography part II—Application," Constr. Build. Mater. **14**(3), 147–156.

Larose, E., and Hall, S. (**2009**). "Monitoring stress related velocity variation in concrete with a $2\times10^{-5}$ relative resolution using diffuse ultrasound," J. Acoust. Soc. Am. **125**, 1853–1856.

Larose, E., De Rosny, J., Margerin, L., Anache, D., Gouedard, P., Campillo, M., and VanTiggelen, B. (**2006**). "Observation of multiple scattering of kHz vibrations in a concrete structure and application to weak changes monitoring," Phys. Rev. E **73**, 016609.

Lobkis, O. I., and Weaver, R. L. (**2003**). "Coda-wave interferometry in finite solids: recovery of P-to-S conversion rates in an elastodynamic billiard," Phys. Rev. Lett. **90**, 254302.

McCann, D. M., and Forde, M. C. (**2001**). "Review of NDT methods in the assessment of concrete and masonry structures," NDT&E Int. **34**, 71–84.

Obermann, A., Froment, B., Campillo, M., Larose, E., Planès, T., Valette, B., Chen, J. H., and Liu, Q. Y. (**2014**). "Seismic noise correlations to image structural and mechanical changes associated with the mw 7.9 2008 Wenchuan earthquake," J. Geophys. Res. **119**(4), 3155–3168, doi:10.1002/2013JB010932.

Obermann, A., Planès, T., Larose, E., and Campillo, M. (**2013**). "Imaging preeruptive and coeruptive structural and mechanical changes of a volcano with ambient seismic noise," J. Geophys. Res. **118**, 1–11, doi:10.1002/2013JB010399.

Ohtsu, M., Okamoto, T., and Yuyama, S. (**1998**). "Moment tensor analysis of acoustic emission for cracking mechanisms in concrete," ACI Struct. J. **95**(2), 87–95.

Page, J., Jones, I. P., Schriemer, H. P., Cowan, M. L., Ping Sheng, and Weitz, D. A. (**1999**). "Diffusive transport of acoustic waves in strongly scattering media," Physica B **263–264**, 37–39.

Payan, C., Quiviger, A., Garnier, V., Chaix, J. F., and Salin, J. (**2013**). "Applying diffuse ultrasound under dynamic loading to improve closed crack characterization in concrete," J. Acoust. Soc. Am. **134**(2), EL211–EL216.

Planès, T. (**2013**). "Imaging local changes in the multiple scattering regime," Ph.D. thesis, University of Grenoble.

Planès, T., and Larose, E. (**2013**). "A review of ultrasonic codawave interferometry in concrete," Cem. Concr. Res. **53**, 248–255.

Planès, T., Larose, E., Margerin, L., Rossetto, V., and Sens-Schonfelder, C. (**2014**). "Decorrelation and phase-shift of coda waves induced by local changes: multiple scattering approach and numerical validation," Wave Random Complex **24**, 99–125.

Popovics, J. S., and Rose, J. L. (**1994**). "A survey of developments in ultrasonic NDE of concrete," IEEE Trans. Ultrason., Ferroelec., Freq. Control **41**, 140–143.

Popovics, J. S., Song, W. J., Ghandehari, M., Subramaniam, K. V., Achenbach, J. D., and Shah, S. P. (**2000**). "Application of surface wave

transmission measurements for crack depth determination in concrete," ACI Mater. J. **97**(2), 127–135.

Quiviger, A., Payan, C., Chaix, J. F., Ganier, V., and Salin, J. (**2012**). "Effect of the presence and size of a real macro-crack on diffuse ultrasound in concrete," NDT&E Int. **45**, 128–132.

Ramamoorthy, S. K., Kane, Y., and Turner, J. A. (**2004**). "Ultrasound diffusion for crack depth determination in concrete," J. Acoust. Soc. Am. **115**, 523–529.

Rossetto, V., Margerin, L., Planès, T., and Larose, E. (**2011**). "Locating a weak change using diffuse waves: Theoretical approach and inversion procedure," J. Appl. Phys. **109**, 034903.

Sens-Schönfelder, C., and Larose, E. (**2008**). "Temporal changes in the lunar soil from correlation of diffuse vibrations," Phys. Rev. E **78**(4, Part 2), 045601.

Sens-Schönfelder, C., and Wegler, U. C. (**2006**). "Passive image interferometry and seasonal variations of seismic velocities at Merapi volcano, Indonesia," Geophys. Res. Lett. **33**, L21302, doi:10.1029/2006GL027797.

Tarantola, A., and Valette, B. (**1982**). "Generalized non-linear inverse problems solved using the least-squares criterion," Rev. Geophys. **20**, 219–232, doi:10.1029/RG020i002p00219.

Vergely, J. L., Valette, B., Lallement, R., and Raimond, S. (**2010**). "Spatial distribution of interstellar dust in the sun's vicinity comparison with neutral sodium-bearing gas," Astron. Astrophys. **518**, A3.

Zhang, Y., Abraham, O., Grondin, F., Loukili, A., Tournat, V., Le Duff, A., Lascoup, B., and Durand, O. (**2013**). "Validation of a thermal bias control technique for coda wave interferometry (CWI)," Ultrasonics **53**, 658–664.